Modulation of skyrmion helicity by competition between Dzyaloshinskii-Moriya interaction and magnetic frustration

Yuheng Liu,[1] Baishun Yang,[2,*] Xiaoyan Guo,[1] Silvia Picozzi,[2] and Yu Yan[1,†]

[1]*Key Laboratory of Physics and Technology for Advanced Batteries (Ministry of Education), Department of Physics, Jilin University, Changchun 130012, China*

[2]*Consiglio Nazionale delle Ricerche (CNR-SPIN), Unità di Ricerca presso Terzi c/o Università "G. D'Annunzio," 66100 Chieti, Italy*

(Received 5 July 2023; revised 18 December 2023; accepted 12 March 2024; published 22 March 2024)

Helicity, one of the degrees of freedom for skyrmions, describing the direction of spin rotation in skyrmions, is of fundamental importance for skyrmion-based potential applications. However, continuously modulating the helicity is challenging. Here, we propose an effective method to control the skyrmion helicity by means of the competition between Dzyaloshinskii-Moriya interaction and exchange frustration in inversion-symmetry-broken frustrated magnets. In the prototypical case of Janus NiClBr, we found a nanometer-sized skyrmion with uniform unconventional helicity of 139°. Moreover, a spin texture phase diagram as a function of strain and out-of-plane magnetic field was illustrated and, most importantly, an unexpected linear change in the helicity from ∼0° to ∼50° and from ∼120° to ∼180° was found in the skyrmion lattice region. As such, the skyrmion Hall effect of Janus NiClBr can be reduced under external field for a critical value of the helicity. These results not only give a feasible method to effectively modulating the skyrmion helicity, but also provide an ideal platform for further investigations on skyrmion helicity-related phenomena.

DOI: 10.1103/PhysRevB.109.094431

I. INTRODUCTION

Magnetic skyrmions [1] are vortexlike swirling spin textures which have been widely observed in chiral [2–5], polar [6–8], and frustrated magnets [9,10] due to competition among magnetic interactions, such as Heisenberg-like exchange coupling, Dzyaloshinskii-Moriya (DM), dipole-dipole, and magnetic anisotropy [11–13]. The unique topologically protected, nanometer-sized and efficient current-driven dynamic properties make the skyrmions appealing candidates for high-stability, low-power, and high-density magnetic data storage and other spintronic applications [14–20]. Driven by their potentials, the knowledge in skyrmions has constantly widened by means of numerous experiments and fundamental theoretical investigations in the last years [16,21–23].

To define a specific skyrmion, three different degrees of freedom, namely topological number Q, vorticity ω, and helicity γ, are used to distinguish the multifarious types of skyrmions. Among them, helicity [24] represents the angle difference between a spin direction and its radial direction. Modulating the degrees of freedom for skyrmions is of fundamental importance for the development of skyrmion-related phenomena and applications [25]. Notably, it was proposed that the helicity could be used to store information for the skyrmion quantum bit [26,27], and have a direct relevance to the skyrmion Hall effect [28–30]. Therefore, helicity offers a rich operation regime for potential skyrmion-based devices and manipulating skyrmion helicity is in demand.

So far, most of the studies are focused on the helicity in some specific systems. On one hand, in centrosymmetry-broken systems, the DM interaction is constrained to certain directions, according to the Moriya rules [31,32]. As a result, the determined DM leads to a certain Lifshitz invariant and the helicity is finally fixed to some conventional value [33,34]. For example, in multilayer magnets with C_{nv} symmetry, the helicity is either 0 or π and the corresponding skyrmions are commonly named as Néel-type skyrmions [6]; Bloch-type skyrmions with $\gamma = \pm\pi/2$ emerge in chiral crystal with D_n symmetry [4], and anti-skyrmions with $\gamma = 0$ or π or $\pm\pi/2$ appear in magnets with D_{2d} and S_4 symmetry [35]. In general, the skyrmion diameter of DM-induced skyrmions is in the order of $10^2 \sim 10^3$ nanometers. On the other hand, in frustrated magnets [36–39], the competing interactions among local spins tend to produce highly degenerate ground states, therefore, under some specific conditions, skyrmions with arbitrary helicity might be generated in frustrated magnets [9,40]. Meanwhile, the skyrmion diameter in frustrated magnets can be as small as several nanometers. Besides, via Lorentz transmission electron microscopy (LTEM) it was observed that chirality reverses in helimagnets $Mn_{1-x}Fe_xGe$ as the chemical composition changes, providing evidence for helicity reversal [41]. Moreover, due to the surface reconstruction, twisted skyrmions arise at the surface of chiral magnets, leading the helicity to gradually change its sign from bottom to top, as directly observed by using circular dichroism in resonant elastic x-ray scattering (CD-REXS) [42]. However, to our knowledge, a homogenous and continuous variation of helicity under external field has not been experimentally achieved yet, therefore limiting the development of skyrmion helicity-related phenomena.

In this manuscript, we propose a method for modulating the skyrmion helicity by applying strain and magnetic

*baishun.yang@spin.cnr.it
†yanyu@jlu.edu.cn

field. Taking the prototype monolayer Janus NiClBr as an example, an unexpected unconventional homogenous helicity is observed in the skyrmion lattice due to the induced DM interaction in this frustrated magnet. Moreover, a rich spin texture phase diagram is achieved by changing the strain and magnetic field. Furthermore, a modulation of the skyrmion helicity is obtained in the skyrmion lattice region; as such, it might be possible to reduce the skyrmion Hall effect under specific circumstances. Notably, the proposed method to modulate the skyrmion helicity can be used in future skyrmion based applications.

II. COMPUTATIONAL METHODS

First principles calculations were performed using the Vienna *ab initio* simulation package (VASP) [43]. The exchange-correlation potential was treated with the Perdew-Burke-Ernzerhof (PBE) approach [44]. The Liechtenstein's method [45] with an effective Hubbard U = 1.8 eV and J = 0.8 eV was used to correct correlation effects of Ni-3*d* orbitals. A plane-wave cutoff energy of 500 eV and a $19 \times 19 \times 1$ Γ-centered k mesh were adopted in all the calculations. To avoid the spurious interlayer interaction arising from the periodic boundary conditions, a 20 Å vacuum region was used. All the atoms were fully relaxed until the force and total energy difference is less than 0.001 eV/Å and 10^{-6} eV, respectively.

We used the four-states approach [46,47] to estimate the magnetic interaction parameters based on first principles calculations for total energies on various spin configurations. In particular, we estimated single ion anisotropy (SIA), first-neighbor and second-neighbor exchange interactions using a $5 \times 4 \times 1$ supercell with k-mesh $4 \times 5 \times 1$ and a $6 \times 3 \times 1$ supercell with k-mesh $3 \times 6 \times 1$ was used for estimating the third-neighbor exchange interaction. Such large supercells exclude any significant influence from next periodic neighbors. Here, we only performed a direct calculation on the magnetic Ni-Ni pair along one selected direction to evaluate the magnetic exchange tensor; in fact, the interactions between the other five same nearest-neighbor pairs can be obtained via the mirror and threefold rotation symmetry.

The Monte Carlo (MC) simulations were performed using the VAMPIRE package [48]. In order to have a better figure arrangement for the spin textures, we change the triangular lattice to a rectangular lattice [see Fig. 2(a)], and x, y, z coordinates are used. The spin texture was calculated with a 12 nm × 12 nm (1360 spins) system. The in-plane periodic boundary condition was used and a randomly distributed spin texture was selected as the initial state. A field cooling method, in which the calculation temperature starts from 30 K and gradually decreases to near 0 K, was adopted in all the calculations. For each simulation, 3×10^6 total calculation steps were performed. The applied external magnetic field is considered along the z direction.

III. RESULTS AND DISCUSSION

A. The idea of modulating skyrmion helicity

The skyrmion helicity is identified as $\gamma = \theta - Q\varphi$, where θ and φ represent the angles for the spin direction and the radial direction relative to the horizontal line for one specific spin in the skyrmion region (see the middle bottom panel in Fig. 1). Q is the topological number for the skyrmions (antiskyrmions) in our manuscript $Q = 1(-1)$. To accurately estimate the helicity, we first find the center of the skyrmion, then calculate the average value of the helicity for all the spins in the skyrmion area by $\gamma = \frac{1}{N}\sum_i (\theta_i - \varphi_i)$, where N is the total number of spins in the skyrmion area. Figure 1 displays a schematic diagram to modulate the skyrmion helicity. Let's focus on an inversion symmetry broken frustrated magnet. On one hand, for some class of centrosymmetric classic frustrated triangle lattices [49,50], skyrmions with arbitrary helicity may appear (see middle skyrmion in Fig. 1 with γ^*). On the other hand, the broken symmetry will induce DM interactions, which will generate conventional helicity in the crystal. Suppose, in some specific polar crystals, the direction of DM to be perpendicular to the connecting line between two arbitrary magnetic atoms A and B, i.e., DM⊥ r_{AB}. An appropriate DM strength will force the spins to form Néel-type skyrmions with the $\gamma = 0$ or π, as shown in the left panel in Fig. 1. Similarly, for chiral crystals where DM//r_{AB}, a moderate DM strength will generate the Bloch-type skyrmion with $\gamma = \pm\pi/2$, as shown in the right panel in Fig. 1. In an intermediate situation, the competition between DM and magnetic frustration might lead to a helicity in the $(0, \pi)$ and $(-\pi/2, \pi/2)$ ranges for polar and chiral crystals, respectively.

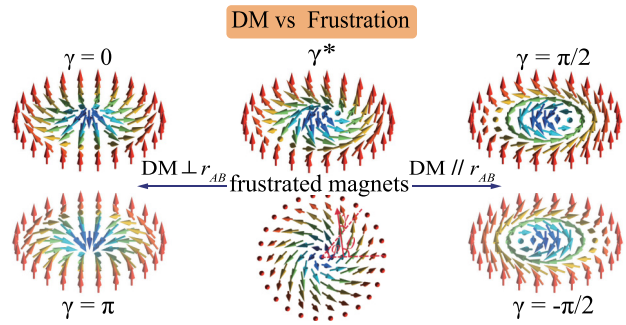

FIG. 1. Schematic diagram of the competition between DM and exchange frustration for generating variation of skyrmion helicity. γ^* in the middle represents arbitrary helicity in frustrated magnets. Left panel: DM perpendicular to the connecting line between two magnetic atoms, $DM \perp r_{AB}$, induces two Néel-type skyrmions. Right panel: DM parallel to the connecting line between two magnetic atoms, $DM//r_{AB}$, induces two Bloch-type skyrmions.

B. Magnetic interactions in prototype nickel halides

Van der Waals (vdW) monolayer nickel halides NiX_2 (X = Cl, Br, I) with space point D_{3d}, are centrosymmetric and demonstrated to be strong frustrated magnets [51]. Based on the prototype NiX_2, we construct Janus NiClBr with space point C_{3v} [see Fig. 2(a)] to induce DM interaction because both the mirror and inversion symmetry are broken in Janus structures. Since the phonon spectrum indicates a monolayer NiClBr to be dynamically stable [52], this might be a good candidate to investigate the competition between DM interaction and exchange frustration. The general spin Hamiltonian model that describes the magnetic interactions between each

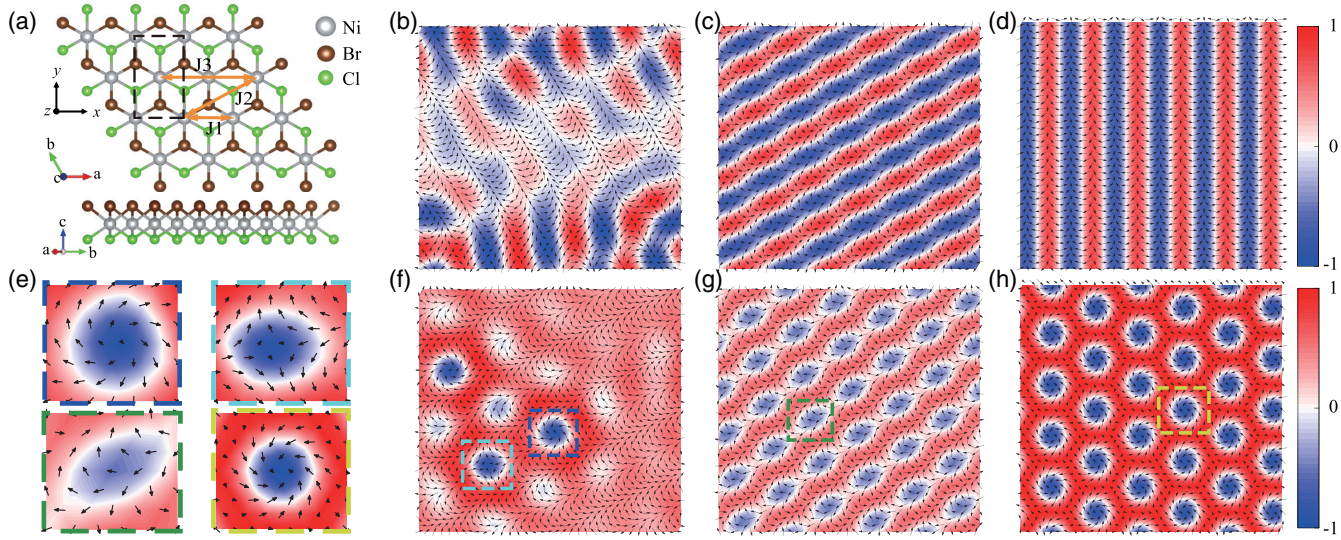

FIG. 2. Real space atomic structure and spin textures. (a) Top and side views of monolayer Janus NiClBr, in which silver, brown, and green balls represent Ni, Br, and Cl atoms, respectively. Spin textures of (b) $NiCl_2$, (c) $NiBr_2$, and (d) NiClBr at zero magnetic field, and spin textures of (f) $NiCl_2$ at μ_{Ni}Bz/J1 = 0.06, (g) $NiBr_2$ at μ_{Ni}Bz/J1 = 0.17, and (h) NiClBr at μ_{Ni}Bz/J1 = 0.26, respectively. (e) Enlarged spin textures for the framed regions in Figs. 2(f)–2(h). The blue-red color scale represents the out-of-plane magnetization, whereas black arrows represent the in-plane spin projections.

local spin pairs is as follows:

$$H = \frac{1}{2}\sum_{i\neq j} S_i \mathrm{J}_{ij} S_j + \sum_i S_i A_i S_i + H_{\mathrm{ext}}, \qquad (1)$$

where, $\boldsymbol{S}_i$ and $\boldsymbol{S}_j$ are spin operators at sites i and j, J_{ij} and A_i represent the exchange coupling interaction and SIA, respectively, and H_{ext} represents the external field energy. All the parameters can be obtained from first principles calculations for Janus NiClBr using the four-states approach. The antisymmetric DM interaction can be calculated from the J_{ij} tensor as $\mathrm{D}_\gamma = \frac{1}{2}\varepsilon_{\alpha\beta\gamma}(\mathrm{J}_{\alpha\beta} - \mathrm{J}_{\beta\alpha})$, where $\varepsilon_{\alpha\beta\gamma}$ is the Levi-Civita symbol. To have a comprehensive understanding on the difference between prototype $NiCl_2$, $NiBr_2$ and the constructed Janus NiClBr, the magnetic parameters of all three materials are calculated and listed in Table I. The first nearest-neighbor isotropic ferromagnetic (FM) interaction $\mathrm{J1} = (\mathrm{J1}_{xx} + \mathrm{J1}_{yy} + \mathrm{J1}_{zz})/3$ for $NiCl_2$, $NiBr_2$, and NiClBr are −6.32, −7.49, and −6.56 meV, respectively. Since J1 shows a nearly isotropic Heisenberg-like interaction, only the isotropic exchange interactions of J2 and J3 are considered in our calculations. Notably, J3 for $NiCl_2$, $NiBr_2$, and NiClBr are antiferromagnetic (AFM) interactions with strengths of 1.98, 3.47, and 2.94 meV, respectively. All the J2 and in-plane SIA are nearly zero. These results indicate that monolayer $NiCl_2$, $NiBr_2$, and NiClBr are classical frustrated magnets, the corresponding frustration strength |J3/J1| being 0.31, 0.46, and 0.45, respectively. Most importantly, at variance with $NiCl_2$ and $NiBr_2$, the DM interaction is induced in the Janus NiCrBr and, following Moriya rules, the DM is in the yz plane with $\mathrm{D}_y = 0.06$ meV and $\mathrm{D}_z = 0.02$ meV.

C. Spin textures in prototype nickel halides

Based on first principles calculations, our atomistic spin simulations are performed with the Monte Carlo method. Figures 2(b)–2(d) illustrate the spin textures under zero external magnetic field μ_{Ni}Bz/J1 = 0 for $NiCl_2$, $NiBr_2$, and NiClBr, respectively, where $\mu_{Ni} = 2.00\mu_B$ represents for the magnetic moment of Ni in $NiCl_2$, $NiBr_2$, and NiClBr. Due to the strong |J3/J1| > 0.25, helicoid spin textures are present. The not-very-regular helicoid structure in $NiCl_2$ arises because the frustration strength is |J3/J1| = 0.31, i.e., near the crossing region between forming skyrmions and spin spiral textures [49,53]. Considering that the skyrmion phase is usually not the ground state, an out-of-plane magnetic field Bz was applied to the three systems. As seen from Figs. 2(f)–2(h), the spin textures are totally different. The frustrated magnet $NiCl_2$ generates both skyrmion [enlarged blue frame in Fig. 2(e)] and antiskyrmion [enlarged light blue frame in

TABLE I. Exchange coupling interactions for first-nearest neighbor J1 tensor, isotropic second-nearest neighbor J2, isotropic third-nearest neighbor J3, and single ion anisotropy (SIA). All the units are meV.

	$\mathrm{J1}_{xx}$	$\mathrm{J1}_{yy}$	$\mathrm{J1}_{zz}$	$\mathrm{J1}_{xy}$	$\mathrm{J1}_{xz}$	$\mathrm{J1}_{yz}$	$\mathrm{J1}_{yx}$	$\mathrm{J1}_{zx}$	$\mathrm{J1}_{zy}$	J2	J3	SIA
$NiCl_2$	−6.31	−6.32	−6.32	0.00	0.00	0.00	0.00	0.00	0.00	−0.11	1.98	0.00
$NiBr_2$	−7.55	−7.22	−7.39	0.00	0.00	−0.18	0.00	0.00	−0.18	−0.23	3.47	0.05
NiClBr	−6.64	−6.48	−6.55	−0.02	0.06	−0.10	0.02	−0.06	−0.10	−0.18	2.94	0.01

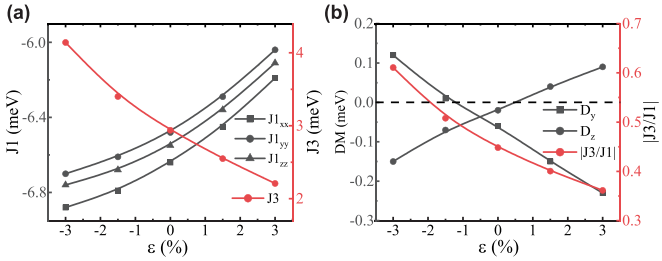

FIG. 3. Exchange parameters as a function of strain ε. (a) Exchange coupling interactions $J1_{xx}$, $J1_{yy}$, $J1_{zz}$, (black curves) and J3 (red curve) as a function of strain. (b) D_y, D_z, (black curves) and frustration strength |J3/J1| (red curve) as a function of strain. The black dashed horizon line indicates the case of DM = 0.

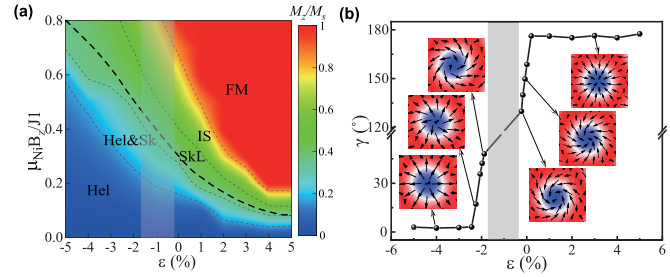

FIG. 4. Skyrmion helicity under strains. (a) Phase diagram of monolayer NiClBr as a function of strain and magnetic field μ_{Ni}Bz/J1, in which blue, green, and red regions represent helicoid, skyrmion lattice, and FM spin textures, respectively. (b) Variation of skyrmion helicity with strain (Insets show the real-space isolated skyrmions at different strains. The shadowed region indicates the "DM-free" region where mainly frustration is at play).

Fig. 2(e)] with unconventional helicity at μ_{Ni}Bz/J1 = 0.06. The calculated skyrmion helicity for the labeled skyrmion and antiskyrmion in Fig. 2(f) is 47° and 146°, respectively. Helicoid spin textures emerge in monolayer $NiBr_2$ at μ_{Ni}Bz/J1 = 0.17 [Fig. 2(g) and enlarged green frame in Fig. 2(e)]. Interestingly, a skyrmion lattice (SkL) is present in Janus NiClBr under μ_{Ni}Bz/J1 = 0.26 even with small in-plane SIA [Fig. 2(h) and enlarged yellow frame in Fig. 2(e)]. Moreover, consistently with our proposed hypothesis in Fig. 1, the helicity of the SkL has a uniform unconventional value of 139° in the frustrated monolayer NiClBr. Furthermore, the diameter of the skyrmion is only 2.8 nm, which is comparable to that in frustrated magnets. In order to find the origin of this uniform unconventional γ in Janus NiClBr, we artificially removed the DM interaction and found that the SkL is absent, no matter how large is the applied Bz. Besides, if the dipole-dipole interaction is included, SkL also emerges at μ_{Ni}Bz/J1 = 0.26 and the skyrmion helicity slightly changes to 144°. Meanwhile, artificially changing the in-plane SIA = 0.01 meV to out-of-plane SIA = −0.01 meV also generates similar SkL spin textures and the corresponding skyrmion helicity slightly changes to 138°. Therefore, we conclude that the DM interaction plays an important role in the uniform unconventional γ in this frustrated magnet.

D. Modulation of skyrmion helicity in NiClBr

Considering the exchange integrals to be strongly sensitive to interatomic distances, to further modulate γ, we applied strain $\varepsilon = (a - a_0)/a_0$, where $a(a_0 = 3.60\,\text{Å})$ denotes the NiClBr lattice constant with (without) strain, to monolayer NiClBr. As shown in Fig. 3(a), the isotropic FM J1 and AFM J3 gradually decrease as the tensile strain increases. The monotonous decrease of the magnitudes of J1 and J3 upon increasing strain is due to the decreasing superexchange integral as the distance between two Ni atoms increases. In order to obtain an intuitive understanding of the DM and frustration in monolayer NiClBr, we plot the strain dependence of D_y, D_z, and frustration strength |J3/J1| in Fig. 3(b). The |J3/J1| ratio keeps decreasing from compressive strain to tensile strain. While the DM interaction is small in the strain region of $-2\% < \varepsilon < 0\%$, its magnitude increases as the tensile or compressive strain increase. SIA keeps lying in-plane with a small value under strain. The variation of the magnetic parameters indicates that competition between DM and magnetic frustration exists under strain and may further modulate the skyrmion helicity in monolayer NiClBr.

To further shed light on the helicity variation under strain, all of the J_{ij} and SIA at different strains need to be obtained. For the J_{ij}, we fit them as a function of strain with the data as shown in Fig. 3 by using a quadratic function; since SIA is nearly absent at all strains, we set SIA = 0. Using the obtained magnetic parameters, we calculated the spin texture phase diagram as a function of μ_{Ni}Bz/J1 and strain by MC simulations, as displayed in Fig. 4(a). Due to the strong frustration and DM interaction at large compressive strain, helicoid spin textures are present under magnetic field μ_{Ni}Bz/J1 < 0.5 [blue region in Fig. 4(a)]. As μ_{Ni}Bz/J1 increases, spins rotate along the Bz direction, generating the skyrmion and SkL. At larger tensile strains, where weak frustration exists, a magnetic field μ_{Ni}Bz/J1 > 0.2 constrains the spins to align out of plane, forming the FM state [red region in Fig. 4(a)]. The spin textures change from helicoid to "helicoid and skyrmion" [Hel and Sk, light blue region in Fig. 4(a)], SkL [green region in Fig. 4(a)], isolated skyrmion [IS, green and yellow region in Fig. 4(a)], and finally to FM states, when the tensile strain and Bz gradually increase. The formation of skyrmions is highly dependent on the specific value of the external magnetic field. We note here that the DM interaction is very small in the shadowed region ($-1.75\% < \varepsilon < -0.25\%$); therefore, due to strong frustration effects, skyrmions display different helicities, thus no homogenous SkL is observed in the shadowed region [see Fig. 5(a)]. Simultaneously, if the in-plane DM, D_y, which can rotate the spins to out of plane, is absent ($\varepsilon \sim -1\%$), and when keeping D_z to a finite value, no matter how large the applied magnetic field, no skyrmions appear, but only helicoid or conoid spin textures are observed [see Fig. 5(b)]. We extract the helicity at the SkL region along the black dashed curve in Fig. 4(b), in which the insets show isolated skyrmions in the SkL at different strains. It is clear that in the region where the DM interaction and frustration are comparable, i.e., except the nearly "DM-free" region (shadowed area), γ linearly changes from ∼0° to ∼50° for $-2.44\% < \varepsilon < -1.88\%$ and from ∼120° to ∼180° for $-0.24\% < \varepsilon < 0.20\%$. Moreover, when the strain is large enough, the DM interaction forces the

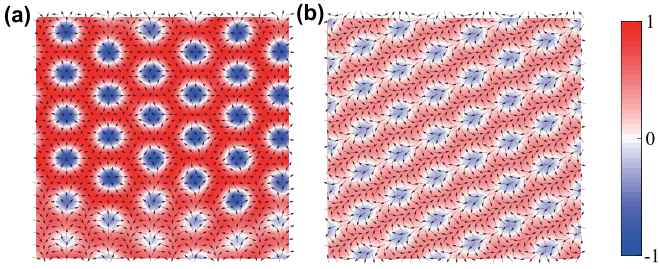

FIG. 5. Spin textures of NiClBr when μ_{Ni}Bz/J1 = 0.26 at (a) $\varepsilon = -1.5\%$ and (b) $\varepsilon = -1.0\%$.

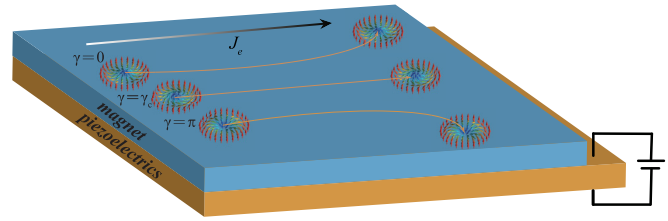

FIG. 6. Schematic diagram of skyrmion motion under electric current J_e for $\gamma = 0$, $\gamma = \gamma_c$, and $\gamma = \pi$ on a device, in which the noncentrosymmetric frustrated magnets like NiClBr are placed on top of piezoelectric materials.

generation of Néel-type skyrmions with helicity ∼0° (∼180°) when $\varepsilon < -2.44\%(\varepsilon > 0.20\%)$. Therefore, it is demonstrated that such an induced variation of homogenous helicity in SkL by competition between frustration and DM can be achieved in monolayer NiClBr by applying strain and magnetic field, and the underlying mechanism is consistent with the schematic diagram shown in Fig. 1. At the same time, we find that the skyrmion diameter keeps a value in the nanometer scale, slightly changing from 1.7 nm at $\varepsilon = -5\%$ to 3.1 nm at $\varepsilon = 5\%$.

E. Skyrmion Hall effect

Due to the Magnus force, the skyrmion Hall effect drives a transverse motion of skyrmions under an applied electric current (J_e), which might destroy the skyrmions in race-track memory devices as shown in Fig. 6. The Hall angle (θ_{Hall}) of skyrmions can be expressed as $\theta_{\text{Hall}} = \tan^{-1}(-Q/\alpha\ D)$, where Q is the topological number, α is the damping constant, $D = \pi^2 d/8\gamma_{dw}$ represents the dissipative tensor, d is the skyrmion diameter, $\gamma_{dw} = \sqrt{A/K}$ represents the width of domain wall, and A and K are the exchange stiffness and magnetic anisotropy, respectively [15]. Therefore, the skyrmion Hall angle can be rewritten as

$$\theta_{\text{Hall}} = \tan^{-1}(-8Q\sqrt{A/K}/\alpha\pi^2 d). \tag{2}$$

Taking the dipole-dipole interaction into consideration and using $\alpha = 0.01$, the calculated $\theta_{\text{Hall}} \sim 84°$ is estimated for unstrained NiClBr. When strain changes from −3% to 3%, the θ_{Hall} changes from 84° to 86° in the skyrmion lattice regions. The real deflection angle of the unconventional skyrmion can be calculated as $\theta_{sk} = \theta_{\text{Hall}} - \gamma$ [28]. Unfortunately, such θ_{Hall} in NiClBr is out of the range for continuous variation of γ from ∼0° to ∼50° for $-2.44\% < \varepsilon < -1.88\%$ and from ∼120° to ∼180° for $-0.24\% < \varepsilon < 0.20\%$. Therefore, the skyrmion Hall effect cannot be eliminated in NiClBr. However, the deflection angle can be reduced to ∼34° when $\varepsilon \sim -1.88\%$. Still, there might exist some other noncentrosymmetric frustrated magnets, where the DM and frustration induced γ is similar to its Hall angle θ_{Hall}. As a result, the skyrmion Hall effect could be eliminated in this magnet.

In order to achieve the skyrmion helicity modulation in experiments, both the magnitude and sign of strain need to be controlled. We design a device, in which the noncentrosymmetric frustrated magnets like NiClBr are placed on top of piezoelectric materials, as schematically shown in Fig. 6. The bias voltage applied to piezoelectric materials results in an out-of-plane electric field, which will lead to an in-plane strain in magnets like NiClBr. The induced strain almost linearly changes with the bias voltage, and the sign of strain reverses when the applied bias voltage changes its direction [54]. Based on this device, the skyrmion helicity in NiClBr could be modulated from ∼0° to ∼50° and ∼120° to ∼180° by the variation of applied bias voltage.

IV. CONCLUSION

In summary, using first principles calculations combined with Monte Carlo simulations, we proposed that the competition between DM interaction and exchange frustration can induce a homogenous helicity in the prototypical Janus NiClBr monolayer. Moreover, we demonstrated that strain is an effective way to modulate the skyrmion helicity from 0 to π. As a result, the skyrmion Hall effect can be reduced by changing the helicity. These results not only provide a powerful method in modulating the skyrmion helicity, but also give a platform for diverse applications based on skyrmion helicity.

ACKNOWLEDGMENTS

Y.Y. acknowledges the financial support from the National Natural Science Foundation of China (Grants No. 12274175 and No. 12261131506) and the Fundamental Research Funds for the Central Universities. S.P. acknowledges financial support from NQSTI within PNRR MUR Project No. PE0000023-NQSTI. The authors acknowledge the computational support provided by the High Performance Computing Center of Jilin University and CINECA via the ISCRA C initiative (Grant No. HP10CJ2EW2).

[1] U. K. Rossler, A. N. Bogdanov, and C. Pfleiderer, Nature (London) **442**, 797 (2006).

[2] M. Bode, M. Heide, K. von Bergmann, P. Ferriani, S. Heinze, G. Bihlmayer, A. Kubetzka, O. Pietzsch, S.

Blugel, and R. Wiesendanger, Nature (London) **447**, 190 (2007).
[3] S. Mühlbauer, B. Binz, F. Jonietz, C. Pfleiderer, A. Rosch, A. Neubauer, R. Georgii, and P. Böni, Science **323**, 915 (2009).
[4] C. Pappas, E. Lelievre-Berna, P. Falus, P. M. Bentley, E. Moskvin, S. Grigoriev, P. Fouquet, and B. Farago, Phys. Rev. Lett. **102**, 197202 (2009).
[5] X. Z. Yu, Y. Onose, N. Kanazawa, J. H. Park, J. H. Han, Y. Matsui, N. Nagaosa, and Y. Tokura, Nature (London) **465**, 901 (2010).
[6] S. Heinze, K. von Bergmann, M. Menzel, J. Brede, A. Kubetzka, R. Wiesendanger, G. Bihlmayer, and S. Blügel, Nat. Phys. **7**, 713 (2011).
[7] I. Kezsmarki, S. Bordacs, P. Milde, E. Neuber, L. M. Eng, J. S. White, H. M. Ronnow, C. D. Dewhurst, M. Mochizuki, K. Yanai, H. Nakamura, D. Ehlers, V. Tsurkan, and A. Loidl, Nat. Mater. **14**, 1116 (2015).
[8] R. Wiesendanger, Nat. Rev. Mater. **1**, 16044 (2016).
[9] A. O. Leonov and M. Mostovoy, Nat. Commun. **6**, 8275 (2015).
[10] C. D. Batista, S. Z. Lin, S. Hayami, and Y. Kamiya, Rep. Prog. Phys. **79**, 084504 (2016).
[11] N. Nagaosa and Y. Tokura, Nat. Nanotechnol. **8**, 899 (2013).
[12] A. Fert, V. Cros, and J. Sampaio, Nat. Nanotechnol. **8**, 152 (2013).
[13] Y. Tokura and N. Kanazawa, Chem. Rev. **121**, 2857 (2021).
[14] C. Hanneken, F. Otte, A. Kubetzka, B. Dupe, N. Romming, K. von Bergmann, R. Wiesendanger, and S. Heinze, Nat. Nanotechnol. **10**, 1039 (2015).
[15] W. Jiang, X. Zhang, G. Yu, W. Zhang, X. Wang, M. Benjamin Jungfleisch, J. Pearson, X. Cheng, O. Heinonen, K. L. Wang, Y. Zhou, A. Hoffmann, and S. G. Velthuis, Nat. Phys. **13**, 162 (2017).
[16] A. Fert, N. Reyren, and V. Cros, Nat. Rev. Mater. **2**, 17031 (2017).
[17] G. Yu, A. Jenkins, X. Ma, S. A. Razavi, C. He, G. Yin, Q. Shao, Q. L. He, H. Wu, W. Li, W. Jiang, X. Han, X. Li, A. C. Bleszynski Jayich, P. K. Amiri, and K. L. Wang, Nano Lett. **18**, 980 (2018).
[18] S. Woo, K. Litzius, B. Krüger, M. Y. Im, L. Caretta, K. Richter, M. Mann, A. Krone, R. M. Reeve, M. Weigand, P. Agrawal, I. Lemesh, M. A. Mawass, P. Fischer, M. Kläui, and G. S. Beach, Nat. Mater. **15**, 501 (2016).
[19] L. Han, C. Addiego, S. Prokhorenko, M. Wang, H. Fu, Y. Nahas, X. Yan, S. Cai, T. Wei, Y. Fang, H. Liu, D. Ji, W. Guo, Z. Gu, Y. Yang, P. Wang, L. Bellaiche, Y. Chen, D. Wu, Y. Nie *et al.*, Nature (London) **603**, 63 (2022).
[20] F. Zheng, H. Li, S. Wang, D. Song, C. Jin, W. Wei, A. Kovacs, J. Zang, M. Tian, Y. Zhang, H. Du, and R. E. Dunin-Borkowski, Phys. Rev. Lett. **119**, 197205 (2017).
[21] K. Everschor-Sitte, J. Masell, R. M. Reeve, and M. Kläui, J. Appl. Phys. **124**, 240901 (2018).
[22] B. Göbel, I. Mertig, and O. A. Tretiakov, Phys. Rep. **895**, 1 (2021).
[23] S. Zhang, G. van der Laan, J. Muller, L. Heinen, M. Garst, A. Bauer, H. Berger, C. Pfleiderer, and T. Hesjedal, Proc. Natl. Acad. Sci. USA **115**, 6386 (2018).
[24] X. Yu, M. Mostovoy, Y. Tokunaga, W. Zhang, K. Kimoto, Y. Matsui, Y. Kaneko, N. Nagaosa, and Y. Tokura, Proc. Natl. Acad. Sci. USA **109**, 8856 (2012).
[25] S. Bhowal and N. A. Spaldin, Phys. Rev. Lett. **128**, 227204 (2022).
[26] C. Psaroudaki and C. Panagopoulos, Phys. Rev. Lett. **127**, 067201 (2021).
[27] J. Xia, X. Zhang, X. Liu, Y. Zhou, and M. Ezawa, Phys. Rev. Lett. **130**, 106701 (2023).
[28] K.-W. Kim, K.-W. Moon, N. Kerber, J. Nothhelfer, and K. Everschor-Sitte, Phys. Rev. B **97**, 224427 (2018).
[29] B. Dai, D. Wu, S. A. Razavi, S. Xu, H. He, Q. Shu, M. Jackson, F. Mahfouzi, H. Huang, Q. Pan, Y. Cheng, T. Qu, T. Wang, L. Tai, K. Wong, N. Kioussis, and K. L. Wang, Sci. Adv. **9**, eade6836 (2023).
[30] H. Vakili, Y. Xie, and A. W. Ghosh, Phys. Rev. B **102**, 174420 (2020).
[31] I. Dzyaloshinsky, J. Phys. Chem. Solids **4**, 241 (1958).
[32] T. Moriya, Phys. Rev. **120**, 91 (1960).
[33] A. Bogdanov and D. Yablonskiui, Sov. Phys. JETP **68**, 101 (1989).
[34] B. Yang, Y. Li, H. Xiang, H. Lin, and B. Huang, Nat. Comput. Sci. **3**, 314 (2023).
[35] A. K. Nayak, V. Kumar, T. Ma, P. Werner, E. Pippel, R. Sahoo, F. Damay, U. K. Rossler, C. Felser, and S. S. P. Parkin, Nature (London) **548**, 561 (2017).
[36] A. P. Ramirez, Annu. Rev. Mater. Sci. **24**, 453 (1994).
[37] L. Balents, Nature (London) **464**, 199 (2010).
[38] B. Normand, Contemp. Phys. **50**, 533 (2009).
[39] O. A. Starykh, Rep. Prog. Phys. **78**, 052502 (2015).
[40] X. Zhang, J. Xia, Y. Zhou, X. Liu, H. Zhang, and M. Ezawa, Nat. Commun. **8**, 1717 (2017).
[41] K. Shibata, X. Z. Yu, T. Hara, D. Morikawa, N. Kanazawa, K. Kimoto, S. Ishiwata, Y. Matsui, and Y. Tokura, Nat. Nanotechnol. **8**, 723 (2013).
[42] S. L. Zhang, G. van der Laan, W. W. Wang, A. A. Haghighirad, and T. Hesjedal, Phys. Rev. Lett. **120**, 227202 (2018).
[43] G. Kresse and J. Furthmüller, Comput. Mater. Sci. **6**, 15 (1996).
[44] J. P. Perdew, K. Burke, and M. Ernzerhof, Phys. Rev. Lett. **77**, 3865 (1996).
[45] S. L. Dudarev, G. A. Botton, S. Y. Savrasov, C. J. Humphreys, and A. P. Sutton, Phys. Rev. B **57**, 1505 (1998).
[46] H. Xiang, C. Lee, H. J. Koo, X. Gong, and M. H. Whangbo, Dalton Trans. **42**, 823 (2013).
[47] D. Šabani, C. Bacaksiz, and M. V. Milošević, Phys. Rev. B **102**, 014457 (2020).
[48] R. F. Evans, W. J. Fan, P. Chureemart, T. A. Ostler, M. O. Ellis, and R. W. Chantrell, J. Phys.: Condens. Matter **26**, 103202 (2014).
[49] Y. A. Kharkov, O. P. Sushkov, and M. Mostovoy, Phys. Rev. Lett. **119**, 207201 (2017).
[50] T. Okubo, S. Chung, and H. Kawamura, Phys. Rev. Lett. **108**, 017206 (2012).
[51] D. Amoroso, P. Barone, and S. Picozzi, Nat. Commun. **11**, 5784 (2020).
[52] T. Gorkan, J. Das, J. Kapeghian, M. Akram, J. V. Barth, S. Tongay, E. Akturk, O. Erten, and A. S. Botana, Phys. Rev. Mater. **7**, 054006 (2023).
[53] S. Hayami, Phys. Rev. B **103**, 224418 (2021).
[54] F. Ding, H. Ji, Y. Chen, A. Herklotz, K. Dörr, Y. Mei, A. Rastelli, and O. G. Schmidt, Nano Lett. **10**, 3453 (2010).